Single-atomic-Co cocatalyst on (040) facet of BiVO₄ toward efficient photoelectrochemical water splitting

Yucong Miao [a], Jingchao Liu [a], Lixun Chen [a], He Sun [a], Ruikang Zhang [b,*], Jian Guo [a,*], Mingfei Shao [a,*]

[a] State Key Laboratory of Chemical Resource Engineering, Beijing University of Chemical Technology, Beijing 100029, China
[b] College of Chemistry and Material Science, Hebei Normal University, Shijiazhuang, Hebei 050024, China

ARTICLE INFO

ABSTRACT

Monoclinic bismuth vanadate (BiVO₄) shows promising application prospect in photoelectrochemical (PEC) water splitting on account of its relatively ideal band gap to harvest sunlight. However, the poor charge migrate property and sluggish water oxidation kinetics severely limit the PEC performance of BiVO₄ photoelectrodes. In this work, BiVO₄ photoanode with highly exposed (040) facets for superior charge transfer was prepared by a seed assisted hydrothermal method. Moreover, cobalt single atoms stabilized in N-doped carbon nanosheet (Co SAs-NC) was well modified on BiVO₄ (040) (denoted as BiVO₄ (040)/Co SAs-NC) with much improved water oxidation efficiency. The as-prepared BiVO₄ (040)/Co SAs-NC photoanode generated 2.2 times higher photo-current density than that of pristine BiVO₄ (040) at 1.23 V *vs.* RHE, and presented nearly 100% charge injection efficiency. The detail kinetic measurements reveal that the modified Co SAs-NC cocatalyst effectively suppresses the carrier recombination and promotes the surface reaction kinetics. This work provides a promising strategy to fabricate composite photoanodes for solar energy conversion based on facet engineering matched with single-atomic-catalyst.

1. Introduction

Photoelectrochemical (PEC) water splitting has drawn much attention in the field of solar energy conversion, which provides a promising route to efficiently harvest and utilize solar energy to generate sustainable hydrogen fuel [1–4]. To achieve this goal, explore promising photoelectrodes for driving cathodic hydrogen evolution reaction (HER) and anodic oxygen evolution reaction (OER) is the critical issue for PEC water splitting. In particular, the sluggish four-electron transfer process of OER demands highly efficient photoanode to block the carrier recombination and accelerate the kinetic of oxidation reaction [5–7]. Up to date, various photoanodes based on the metal oxide semiconductors (e.g., TiO₂ [8], ZnO [9,10], WO₃ [11], Fe₂O₃ [12,13], and BiVO₄ [14–16]) have been investigated with the purpose of high H₂ production yield by improving the light adsorption, charge generation and utilization efficiency. Among these photoanodes, monoclinic bismuth vanadate (BiVO₄) has been intensively studied due to its relatively ideal band gap to harvest sunlight [17–19]. However, poor charge carrier migrate property and sluggish water oxidation kinetic limits its PEC performance

[20–22], making it a challenge to fabricate BiVO₄ based photoanode with high charge separation and charge injection efficiencies.

Facet orientation of semiconductor crystals can dramatically affect charge migration processes owing to the anisotropic facets with different atomic coordination and arrangement [23–25]. It is reported that the photo-generated electrons preferentially migrate to (0 0 1) facets while holes preferentially gather on (1 1 0) facets of SrTiO₃ nanocrystal [26]. However, the high chemical reactivity facets are always hard to be fabricated because of high surface energy, which makes it unstable in a conventional environment [27,28]. For instance, the (040) facets of BiVO₄ are not preferentially grown crystal surface, but show higher PEC activity [29], which makes it a challenge to control the BiVO₄ photoanode with exposed active facet. On the other hand, the proper contact between BiVO₄ exposed facet and modified layer is also crucial to increase the density of separated electron–hole pairs [30,31]. For example, making an intimate close contact between BiVO₄ and the black phosphorene can more easily construct an electric field from the p/n junctions to separate carriers [32]. It is reported that the poor semiconductor/cocatalyst interface may introduce new recombination sites

---

of charge carriers that hindered the PEC performances [33–35]. Thus, it is prospective that loading a small amount of cocatalysts on photoanode can bring sufficient reaction sites but not influence crystal structure or break the transfer of charge carriers.

Recently, single atom catalysts have been reported with remarkable catalytic activity for energy conversions [36–39], which provide opportunity to build ideal semiconductor/cocatalyst interface of photoanodes for efficient PEC water splitting. For instance, Y. Pang and co-workers [40] assembled bismuth single atoms on TiO_2 nanorods photoanode, which indicated that a small amount of Bi single atoms loading can significantly prolong the electron lifetime while reducing the interface charge transfer resistance. Herein, we display the controlled synthesis of $BiVO_4$ grown on the conducting substrate with highly exposed (040) facet, which is further modified by using cobalt single atoms stabilized in N-doped carbon nanosheet (denoted as $BiVO_4$ (040)/Co SAs-NC). The as-developed $BiVO_4$ (040)/Co SAs-NC photoanode demonstrates 2.2 times higher photocurrent density than that of the pristine $BiVO_4$ (040). In addition, $BiVO_4$ (040)/Co SAs-NC shows nearly 100% charge injection efficiency at 1.23 V *vs.* RHE, implying the ideal semiconductor/cocatalyst interface and high OER catalytic activity of Co SAs-NC. The Mott–Schottky measurements, time-resolved transient photoluminescence and electrochemical impedance spectroscopy (EIS) further reveal that Co SAs-NC facilitates the interface charge transfer and charge injection in $BiVO_4$ (040)/Co SAs-NC composite photoanode.

2. Experimental sections

2.1. Preparation of BiVO₄ (040) photoanodes

The $BiVO_4$ seed layer fabricated on a FTO glass substrate was performed in the light of a previously reported method [41]. And the synthesis process for $BiVO_4$ (040) photoanode was improved from that reported by Li et al [42]. For a typical synthesis procedure, 8 mL of 2.0 M NaOH aqueous solution with 11.698 mg NH_4VO_3 and 8 mL of 2.0 M HNO_3 aqueous solution contained 48.507 mg $Bi(NO_3)_3·5H_2O$ were mixed together, followed by adding concentrated nitric acid until the pH value becomes 0.9. Then the solution was filled into a stainless steel autoclave with a PTFE liner with a capacity of 25 mL. Hydrothermal growth was performed at 180 °C for different hours, where the optimal value was 3 h. The produced photoanode was then calcined for 2 h at 450 °C. $BiVO_4$ (040) below in this work refers to the photoanode under hydrothermal growth of 3 h.

2.2. Preparation of BiVO₄ (040)/Co SAs-NC and BiVO₄ (040)/Co NPs-NC photoanodes

$BiVO_4$ (040)/Co SAs-NC was prepared firstly by electrochemical synthesis of CoZn-zeolitic imidazolate framework (CoZn-ZIF) on the surface of $BiVO_4$ (040) facet. Typically, electrochemical synthesis of ZIF precursor was conducted on a three-electrode cell with $BiVO_4$ (040) photoelectrode as the working electrode, Pt wire as the counter electrode, and Ag/AgCl as the reference electrode. The electrolyte for electrochemical synthesis of ZIF-CoZn (Co: Zn = 1:9) films was prepared by adding an aqueous solution containing 2-methylimidazole (2-MIM) (40 mL, 2.627 g) into 40 mL aqueous solution containing 1.339 g Zn $(NO_3)_2·6H_2O$ + 0.116 g $Co(NO_3)_2·6H_2O$, and the ZIF film was growth under a potential of −1.0 V *vs.* Ag/AgCl. After that, the $BiVO_4$ (040)/ZIF-CoZn was pyrolyzed for 3 h at 450 °C under N_2 atmosphere.

Co nanoparticles on nitrogen-doped carbon nanosheets on the (040) facet of $BiVO_4$ photoanode (denoted as $BiVO_4$ (040)/Co NPs-NC) was prepared with a similar method. The precursors were synthesized by electrochemical synthesis of ZIF-67 (Co: Zn = 1:0). The electrolyte for electrochemical synthesis of ZIF-67 (Co: Zn = 1:0) films was conducted by adding 1.164 g $Co(NO_3)_2·6H_2O$ instead of 1.339 g $Zn(NO_3)_2·6H_2O$ + 0.116 g $Co(NO_3)_2·6H_2O$.

2.3. Photoelectrochemical measurements

The PEC measurements were carried out in a quartz cell of the three-electrode configuration with Pt wire counter electrode and Ag/AgCl reference electrode. The 0.1 M phosphate buffer solution (PBS, pH = 7) was filled in quartz cell, which was also irradiated under simulated solar illumination (AM 1.5 G, 100 mW cm^{-2}) with a 300 W Xenon lamp. The potential range of linear sweep voltammograms (LSV) were from −0.4 to 1.2 V *vs.* Ag/AgCl. The sweep rate was 20 mV s^{-1}.

Electrochemical impedance spectroscopy (EIS) was performed at 1.23 V *vs.* RHE with a frequency between 100 kHz and 0.1 Hz and 0.1 V amplitude of perturbation under illumination.

3. Results and discussion

3.1. Materials preparation and characterization

Scheme 1 illustrated the preparation process of the $BiVO_4$ (040)/Co SAs-NC photoanode. $BiVO_4$ seed layer was prepared by electrosynthesis Bi metal layer on FTO substrate and followed with thermal transition of VO $(acac)_2$ and Bi to $BiVO_4$ (Fig. S1). Then, (040)-crystal facet oriented $BiVO_4$ photoelectrode (denoted as $BiVO_4$ (040)) was hydrothermally synthesized based on the seed layer. ZIF-CoZn (Co: Zn = 1:9) precursor nanosheets were *in-situ* grow on $BiVO_4$ (040) by our previous method [44]. After following pyrolysis process, cobalt single atoms on nitrogen-doped carbon nanosheet were achieved in $BiVO_4$ (040)/Co SAs-NC. The mechanism of Co single atom formation is that the excess zinc ions tend to isolated cobalt ion in ZIF-CoZn, then Zn will evaporate in pyrolysis while Co is reduced by the surrounding organic linker to form a Co–N bond [45]. In order to give a comparison study, cobalt nanoparticles on nitrogen-doped carbon nanosheet was also prepared by pyrolysis of ZIF-67 (without Zn) precursor on $BiVO_4$ (040) photoanode (denoted as $BiVO_4$ (040)/Co NPs-NC).

Fig. 1a shows X-ray diffraction (XRD) patterns of $BiVO_4$ (040) photoanode, and the diffraction peaks corresponding to the monoclinic scheelite $BiVO_4$ (JCPDS#14-0688). As illustrated in Fig. S2, the peak intensity of (−121) plane is about 4 times that of (040) plane in the conventional XRD patterns of $BiVO_4$ card. The peak at 30.5° corresponding to (040) facet of $BiVO_4$ is much stronger than the (−121) facet after hydrothermal treatment, confirming the successful synthesis of $BiVO_4$ with the preferable orientation of (040) facet. After modifying with Co SAs-NC, no new metal peak presence for $BiVO_4$ (040)/Co SAs-NC indicates the monodisperse of Co metal (Fig. 1a). In contrast, $BiVO_4$ (040) modified with Co NPs-NC photoanode presents additional diffraction peak at 2θ 44°, which is ascribed to (111) plane of face-centered cubic Co crystals [46]. Top and cross-sectional scanning electron microscopy (SEM) images of $BiVO_4$ (040) photoanode reveal that $BiVO_4$ microplates with well-defined crystal facets are grown paralleled on the FTO substrate (Fig. 1b). The average size of microplates and the film thickness is about 2.5 and 5 μm, respectively. ZIF-CoZn precursor with 40–60 nm width nanosheet were vertically grown on $BiVO_4$ surface (Fig. S3). After pyrolysis process, it has a shrink and adheres to the (040) facets of $BiVO_4$ along with the transformation of ZIF-CoZn to Co SAs-NC (Fig. 1c). The energy dispersive X-ray (EDX) mapping image of as-prepared $BiVO_4$ (040)/Co SAs-NC photoanode was displayed in Fig. S4a, which indicates the existence of Bi, O, V, C, N and Co elements. EDX spectrum further verified the presence of the above elements, except for Co (Fig. S4b), which may be due to the extremely low loading amount of cobalt in the form of single atoms. Transmission electron microscope (TEM) images show that no Co NPs were found in $BiVO_4$ (040)/Co SAs-NC (Fig. 1d), further suggesting the atomic disperse of Co. In the selected area electron diffraction (SAED) pattern, the polycrystalline nature of $BiVO_4$ (040) was confirmed by observed diffraction rings (Fig. 1f), which can be assigned to the (040) and (−121) planes of $BiVO_4$ (040)/Co SAs-NC. The high-resolution transmission electron microscopy (HRTEM) gives the lattice fringes with the spacing of 0.292 nm
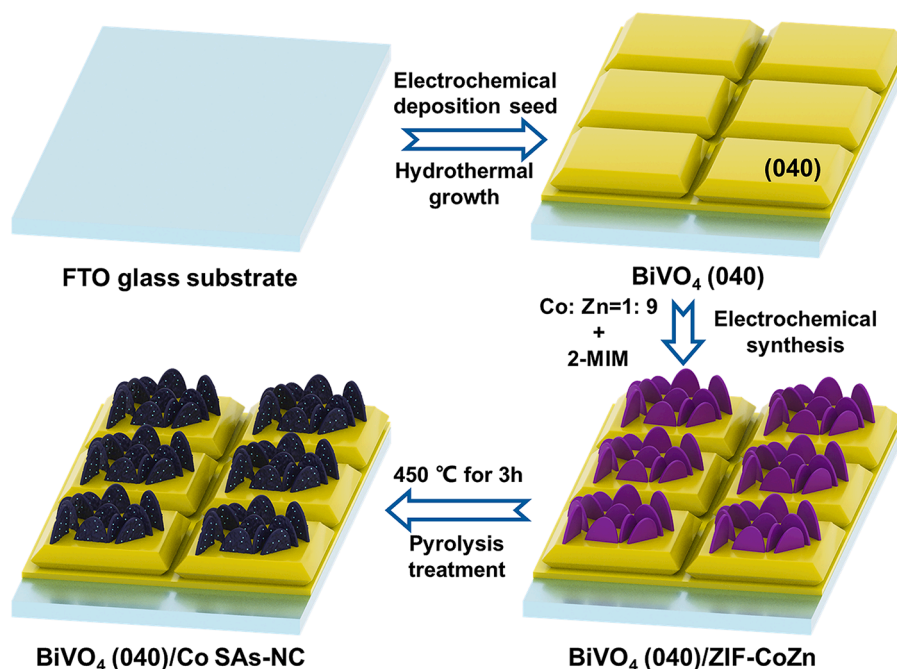
Scheme 1. Schematic illustration for the fabrication of $BiVO_4$ (040)/Co SAs-NC photoanode.

can be indexed to the $BiVO_4$ (040) plane (Fig. 1g) [47]. Subsequent FFT-transformation of Fig. 1g further verified the existence of (040) plane (Fig. 1h). Moreover, the atomic-resolution high angle annular dark-field scanning transmission electron microscope (HAADF-STEM) image of $BiVO_4$ (040)/Co SAs-NC preliminarily verified the existence of Co single atoms (Fig. 1i). For reference sample of $BiVO_4$ (040)/Co NPs-NC, a great quantity of cobalt nanoparticles was distributed on the N-doped carbon nanosheets (Fig. S5).

XPS analysis is conducted to reveal the chemistry and bonding states at surface in $BiVO_4$ (040)/Co NPs-NC and $BiVO_4$ (040)/Co SAs-NC photoanodes (Fig. S6). Fig. 2a shows the high-resolution XPS spectrum for Co 2p. Two peaks at 782.8 and 795.1 eV can be observed in $BiVO_4$ (040)/Co SAs-NC, which is attributed to Co–N_x [45]. In contrast, the characteristic peak of Co metal $2p_{3/2}$ for $BiVO_4$ (040)/Co NPs-NC is observed, indicating the existence of metallic state. The XPS spectrum for N 1s reveals that graphitic-N, pyrrolic-N, Co–N_x and pyridinic-N are composited of nitrogen species in N-doped carbon nanosheets (Fig. 2b). Moreover, the coordination environment of single-atom-Co in $BiVO_4$ (040)/Co SAs-NC was verified by XAS with cobalt phthalocyanine (CoPc) and Co foil as reference samples. The X-ray absorption near-edge structure (XANES) spectra of $BiVO_4$ (040)/Co SAs-NC is distinctly different from that of Co foil, demonstrating the absence of Co metal (Fig. 2c). The pre-edge peak of $BiVO_4$ (040)/Co SAs-NC at 7710 eV is ascribed to the transition of electrons from core 1s orbitals to unoccupied 3d orbitals of the cobalt atoms [48], which indicates its symmetrical tetrahedral structure. The XANES spectra of CoPc show peaks located at 7714–7716 eV, deriving from 1s to 4p electron transition in Co–N_4 square-planar structures [49]. The existence of peak at 7710 eV and the absence of fingerprint peaks of Co–N_4 in $BiVO_4$ (040)/Co SAs-NC both implies its nonplanar structures in Co SAs. The Fourier transforms k^3-weighted extended X-ray absorption fine structure (EXAFS) of $BiVO_4$ (040)/Co SAs-NC exhibits peak at 1.46 Å, which is assigned to the isolated Co–N bonds (Fig. 2d) [50]. The absence of Co–Co bonding located at around 2.18 Å further confirms the evolution of single atoms in $BiVO_4$ (040)/Co SAs-NC. These characterizations indicate that Co is single-atomically dispersed and stabilized by isolated Co–N bonds on the N-doped carbon nanosheet. All the above results adequately prove the successful fabrication of $BiVO_4$ (040)/Co SAs-NC.

3.2. Studies on enhanced PEC performances

The PEC water oxidation measurements were carried out with a three-electrode system in 0.1 M phosphate buffer solution (pH = 7). The LSV measurement in Fig. 3a shown that the photocurrent density of $BiVO_4$ (040)/Co SAs-NC photoanode reaches 0.69 mA cm^{-2} at 1.23 V *vs.* RHE, 2.2 and 1.5 times higher than that of the pristine $BiVO_4$ (040) and $BiVO_4$ (040)/Co NPs-NC, respectively. The onset potential of Co SAs-NC and Co NPs-NC modified photoanodes both reduced from ~0.47 V to ~0.35 V compared to pristine $BiVO_4$ (040) photoanode (Fig. 3b). Moreover, transient photocurrent tests under intermittent light were performed (Fig. 3c). The prompt and reproducible photocurrent response of the three samples suggests the fast light response. What can be clearly observed is that the photocurrent spikes of $BiVO_4$ (040)/Co SAs-NC photoanode almost disappeared during the ON–OFF cycles of the irradiation signal, suggesting that Co SAs facilitates the utilization of accumulated carriers [51]. Moreover, the applied bias photon-to-current conversion efficiency (ABPE) was calculated based on the photo-current–voltage curves (Fig. 3d). The maximum ABPE of $BiVO_4$ (040)/Co SAs-NC photoanode was 0.15% at 0.82 V, shown significantly enhancement than that of $BiVO_4$ (040)/Co NPs-NC (0.10%) and pristine $BiVO_4$ (040) (0.04%). The above results indicate that $BiVO_4$ (040)/Co SAs-NC exhibits the best PEC performance in the as-prepared three samples.

In addition, pure $BiVO_4$ with different exposure degrees of (040) facets can be obtained by regulating hydrothermal duration. Six $BiVO_4$ samples with hydrothermal times of 1, 2, 3, 6, 9, and 12 h were prepared respectively (Fig. S7). We set (040)/(−1 2 1) intensity ratio in the XRD patterns to represent the exposure degree of (040) facets. $BiVO_4$ photoanode with hydrothermal time of 3 h shows the highest (040)/(−1 2 1) ratio value (Fig. S8). Moreover, the PEC performance of as-fabricated $BiVO_4$ photoanodes positively correlated to the intensity ratio of (040)/(−1 2 1), indicating the high PEC oxidation activity of (040) facets (Fig. S9). In addition, the Co SAs-NC cocatalyst loading amount on $BiVO_4$ can be facilely regulated by controlling the electrosynthesis time of ZIF-CoZn precursor. The ZIF nanosheets grow thicker and bigger as increase of deposition time (Fig. S10). The electrochemical measurements of four samples with ZIF precursor deposition time of 10, 20, 30 and 40 s are shown in Fig. S11. In the dark, the $BiVO_4$ (040)/Co SAs-NC
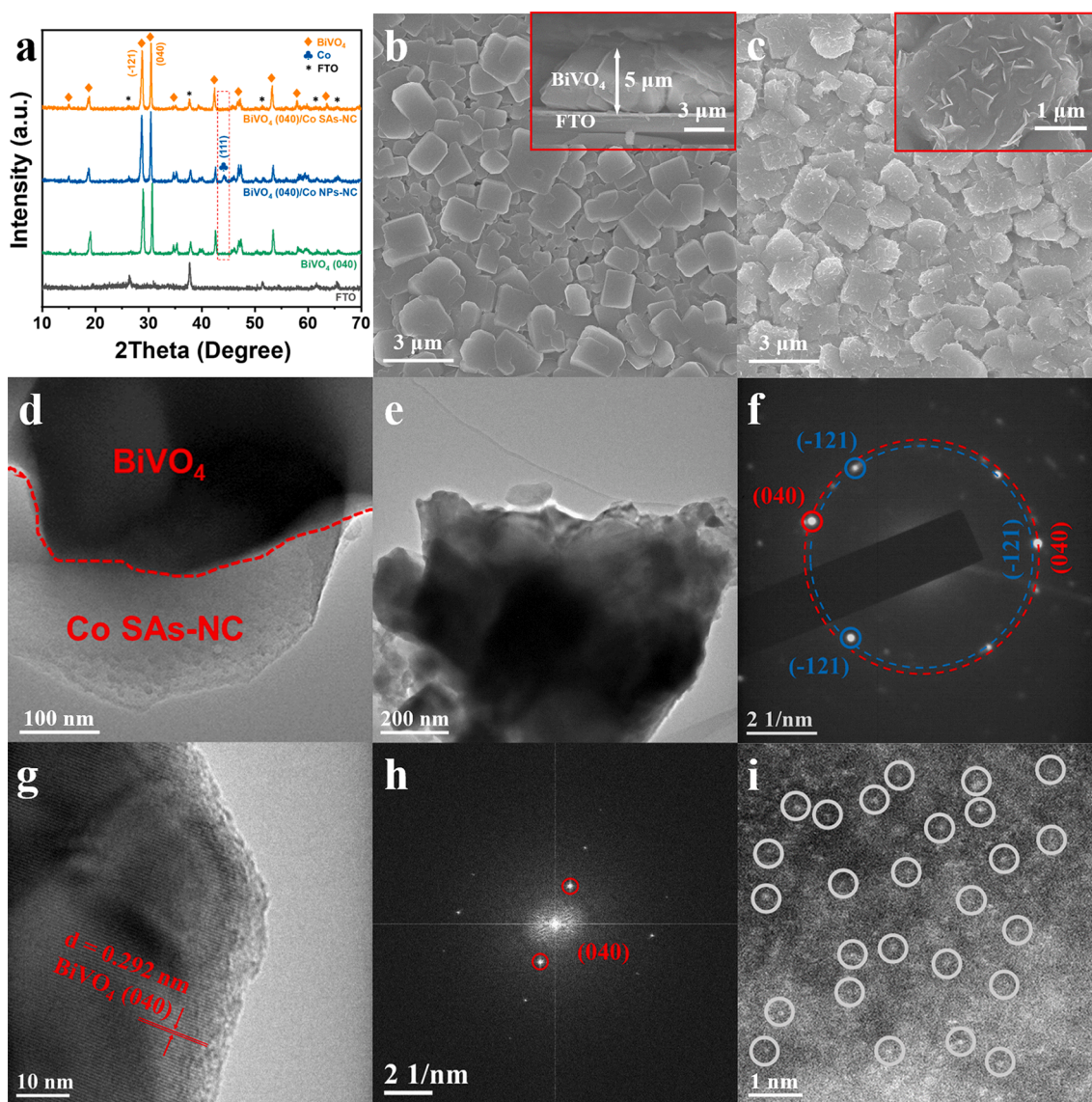
Fig. 1. (a) XRD patterns of FTO substrate, BiVO$_4$ (040), BiVO$_4$ (040)/Co NPs-NC and BiVO$_4$ (040)/Co SAs-NC. (b) SEM images with top and cross-sectional views (inset) of BiVO$_4$ (040) photoanode. (c) SEM and (d) TEM images, (e) TEM image and (f) SAED pattern (selection area is Fig. 1e), (g) HRTEM image and (h) FFT-transformation pattern (selection area is Fig. 1g), (i) HAADF-STEM image of BiVO$_4$ (040)/Co SAs-NC photoanode.

photoanode with deposition time of 40 s presents the best electro-chemical water oxidation reaction, indicating that Co SAs-NC is an effective OER cocatalyst. But under illumination, composite photoanode with deposition time of 20 s showed the best PEC activity. This implies that Co SAs-NC at high loading amount could also act as charge recombination centres, resulting in the decrease of PEC activity. Thus, BiVO$_4$ (040)/Co SAs-NC or BiVO$_4$ (040)/Co NPs-NC with 20 s deposition of ZIF-CoZn precursor were selected to prepare the relevant composite photoanodes.

4. Mechanism discussion

The optical properties of BiVO$_4$ (040), BiVO$_4$ (040)/Co NPs-NC and BiVO$_4$ (040)/Co SAs-NC were investigated by UV–vis diffuse reflectance spectroscopy and photoluminescence (PL) emission spectra. The spectra in Fig. 4a exhibited that the absorption edge of BiVO$_4$ (040)/Co NPs-NC and BiVO$_4$ (040)/Co SAs-NC was basically same with BiVO$_4$ (040), indicating the low loading of Co-NC cocatalyst. The PL emission peak at 535 nm displayed by pristine BiVO$_4$ (040) photoanode was rather strong, corresponding to the recombination of holes and electrons of

BiVO$_4$. The PL intensity of BiVO$_4$ (040)/Co NPs-NC and BiVO$_4$ (040)/Co SAs-NC photoanode has a significant decline, indicating that the loading of Co cocatalysts suppresses recombination of photogenerated charge carriers, while the cobalt in the form of a single atoms has a better effect than nanoparticles. The charge separation efficiency and surface charge injection efficiency are further investigated using H$_2$O$_2$ as holes scavenger (Fig. S12), and the results are shown in Fig. 4c and 4d. The charge separation efficiencies of BiVO$_4$ (040)/Co SAs-NC slightly improved, demonstrating that the charge separation property of original BiVO$_4$ has been relatively limited impacted by loading cocatalysts. In contrast to the above, the charge injection efficiency of BiVO$_4$ (040)/Co SAs-NC is calculated to be 99.47% at 1.23 V *vs.* RHE, which has significant improvement compared to pristine BiVO$_4$ (040) (53.26%) and BiVO$_4$ (040)/Co NPs-NC (69.73%). This suggests that Co SAs-NC can dramatically promote surface water oxidation kinetics.

Due to the unsatisfactory charge separation efficiency, it is necessary to increase the calcination temperature of the photoanode to explore whether the increase in crystallinity can further improve the efficiency of the photoanode. As shown in Fig. S13a, the photoanode calcined at 600 °C all show improved charge separation efficiency, while the charge
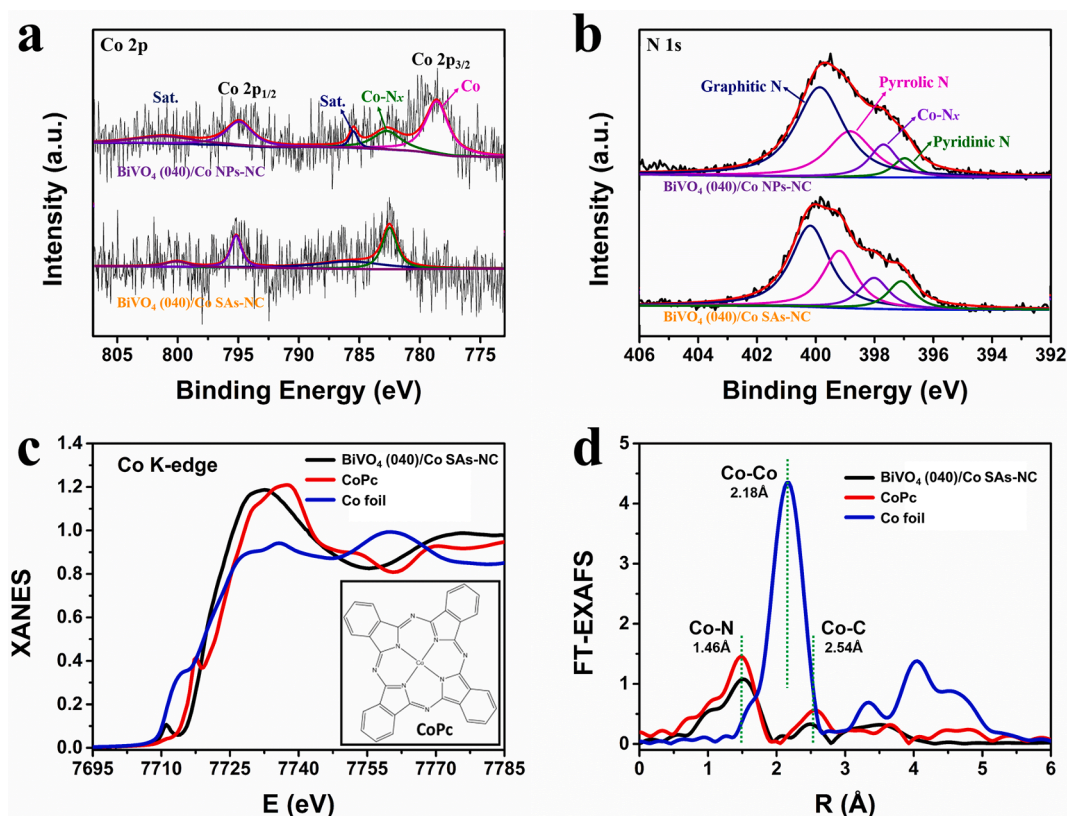
Fig. 2. XPS spectra of (a) Co 2p and (b) N 1s for $BiVO_4$ (040)/Co NPs-NC and $BiVO_4$ (040)/Co SAs-NC. (c) Co K-edge XANES and (d) the corresponding Fourier transforms EXAFS spectra of $BiVO_4$ (040)/Co SAs-NC, CoPc and Co foil.
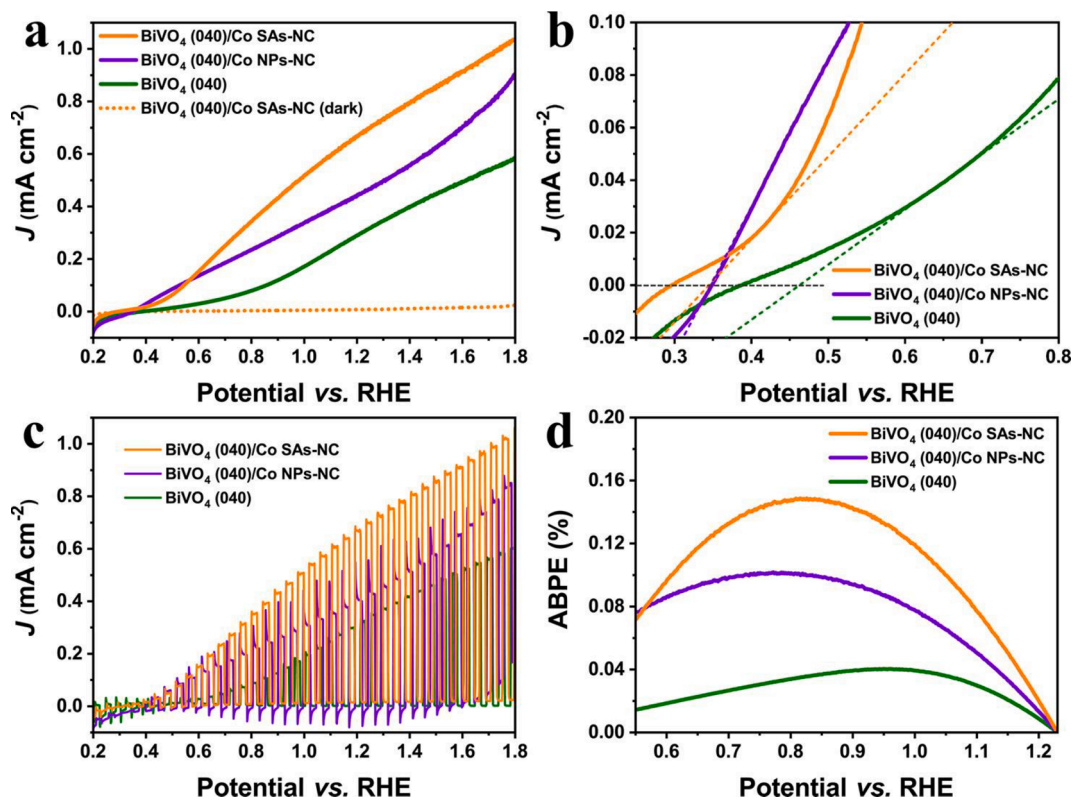
Fig. 3. (a) Photocurrent–potential curves for $BiVO_4$ (040), $BiVO_4$ (040)/Co NPs-NC, $BiVO_4$ (040)/Co SAs-NC and $BiVO_4$ (040)/Co SAs-NC under dark environment, respectively. (b) enlarged image of photocurrent–voltage curves, (c) photocurrent–potential curves under intermittent illumination and (d) ABPE–potential curves for $BiVO_4$ (040), $BiVO_4$ (040)/Co NPs-NC and $BiVO_4$ (040)/Co SAs-NC, respectively.
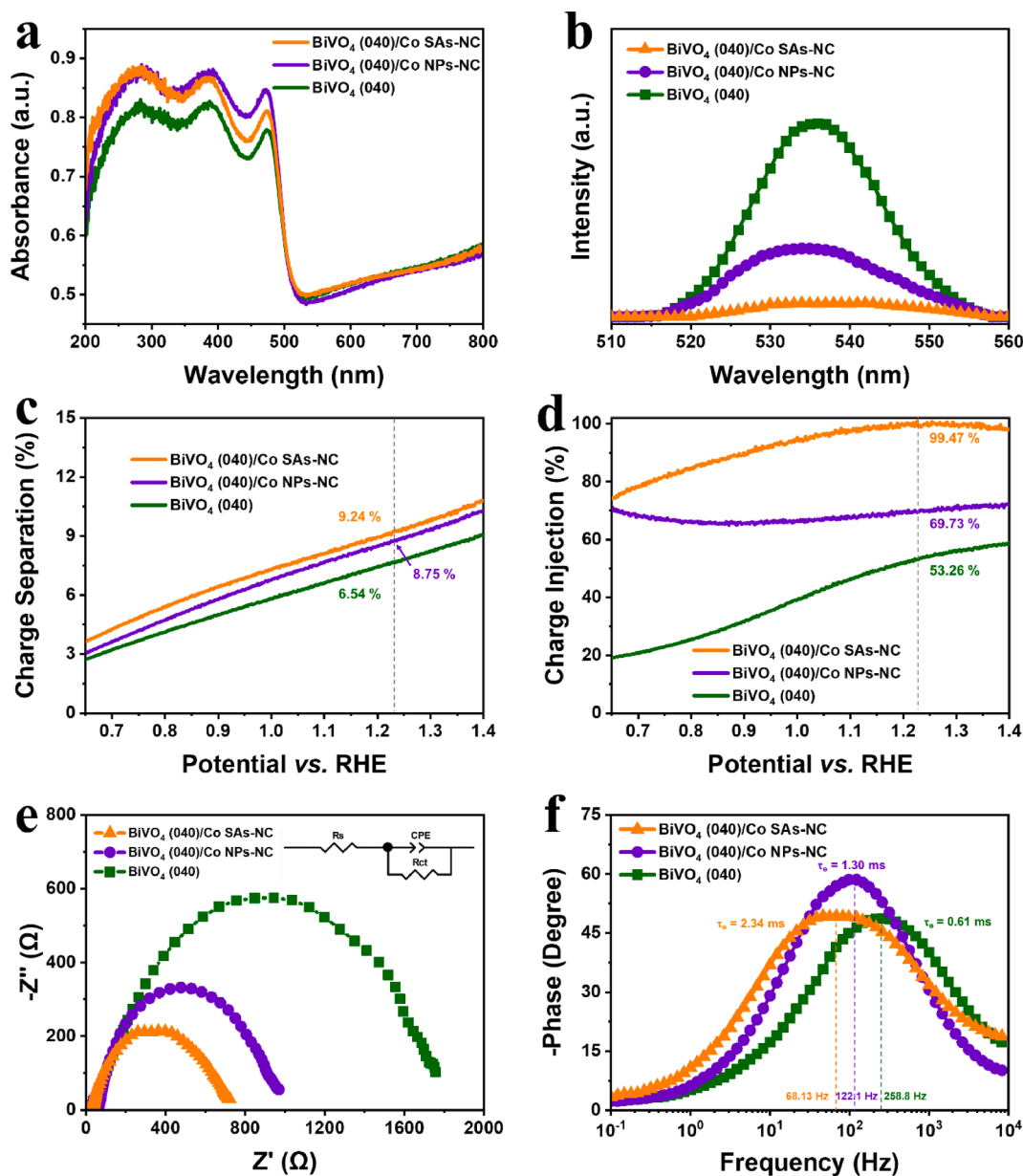
Fig. 4. (a) UV–vis diffuse-reflectance spectra, (b) PL spectra, (c) charge separation efficiency, (d) charge injection efficiency, (e) EIS measured at 1.23 V *vs.* RHE (insert is equivalent circuit model) and (f) Bode phase plots for BiVO$_4$ (040), BiVO$_4$ (040)/Co NPs-NC and BiVO$_4$ (040)/Co SAs-NC, respectively.

injection efficiency is significantly decreased (Fig. S14). The XRD patterns of Fig. S15a shows that the (040)/(−1 2 1) intensity ratio of BiVO$_4$ (040)/Co SAs-NC calcined under 600 °C is declined, which is consistent with the result of SEM images (Fig. S15b and S15c). It is confirmed that the high exposure of (040) facet is a necessary factor to ensure the hole utilization efficiency.

The EIS measurements were performed to investigate the charge transfer behaviors. The equivalent circuit fitting of the EIS Nyquist plot (Fig. 4e) can get R_{ct} and R_s, which represent the interface charge transfer resistance and series resistance respectively [14]. The R_s of each sample are similar, while the R_{ct} of BiVO$_4$ (040)/Co NPs-NC (875.1 Ω) is smaller than that of BiVO$_4$ (040) (1833 Ω), which implied preferable charge transport by introducing Co NPs-NC. This can be ascribed to the quick charge transport to cocatalyst with following enhanced OER kinetics. Furthermore, the BiVO$_4$ (040)/Co SAs-NC photoanode displays the minimum charge transfer resistance (679.4 Ω), indicating the fastest interface charge transfer kinetics. In addition, the electron lifetime (τ_e) was calculated from Bode phase plots (Fig. 4f) [43]. The τ_e values were

0.61 ms, 1.30 ms and 2.34 ms corresponding to BiVO$_4$ (040), BiVO$_4$ (040)/Co NPs-NC and BiVO$_4$ (040)/Co SAs-NC photoanodes, respectively. The long electron lifetime in BiVO$_4$ (040)/Co SAs-NC also implies that Co SAs-NC can facilitate the interfacial charge transfer.

The charge recombination behavior of three samples was investigated by chronoamperometry (Fig. 5a). Anodic photocurrent spike (I_{in}) and stabilized photocurrent (I_{st}) are associated with the accumulation of photogenerated electrons. To quantitatively determine the charge recombination behavior, the transient decay rate (D) and decay time (τ_D) were calculated to reflect the charge recombination [52]. The Fig. 5b shows that the τ_D of BiVO$_4$ (040)/Co SAs-NC photoanode is 2.0 s, which is longer than 0.6 s of BiVO$_4$ (040) and 1.0 s of BiVO$_4$ (040)/ Co NPs-NC. The long τ_D for BiVO$_4$ (040)/Co SAs-NC photoanode demonstrates lower charge carrier recombination rate. To gain insight into the photogenerated charge carrier kinetics, the time-resolved transient photoluminescence measurements were carried out (Fig. 5c). The average fluorescence lifetime values are determined to be 1.10, 1.16 and 1.98 ns for BiVO$_4$ (040), BiVO$_4$ (040)/Co NPs-NC and BiVO$_4$ (040)/Co
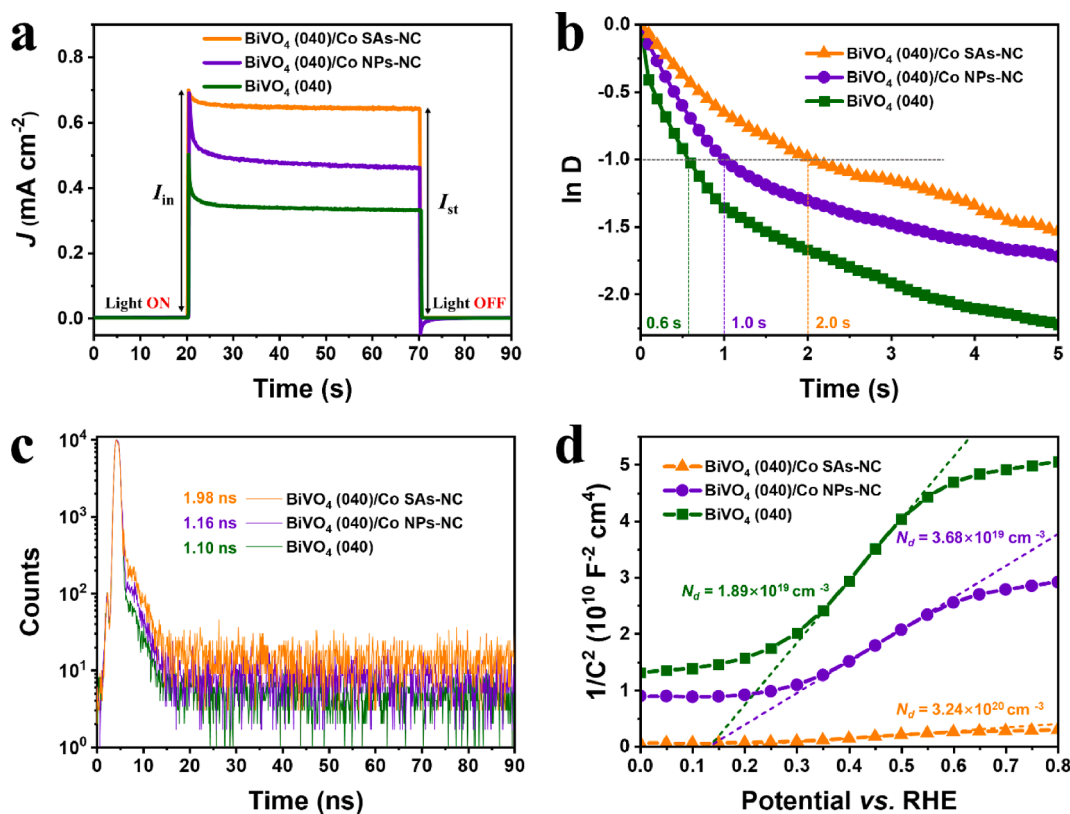
Fig. 5. (a) Transient photocurrent responses at 1.23 V *vs*. RHE, (b) normalized plots of the current–time dependence for the anodic transients, (c) time-resolved transient photoluminescence and (d) Mott-Schottky plots collected at a frequency of 1 kHz in dark for BiVO$_4$ (040), BiVO$_4$ (040)/Co NPs-NC and BiVO$_4$ (040)/Co SAs-NC, respectively.

SAs-NC photoanodes, respectively. The prolonged fluorescence lifetime of BiVO$_4$ (040)/Co SAs-NC demonstrates the long life of minority charge carriers due to the rapid utilization of holes in Co SAs cocatalyst. Long life of excited charge carriers in BiVO$_4$ (040)/Co SAs-NC should bring about high carrier density (N_d), which is estimated by Mott–Schottky measurement (Fig. 5d). It is calculated to be 1.89×10^{19}, 3.68×10^{19} and 3.24×10^{20} cm^{-3} for BiVO$_4$ (040), BiVO$_4$ (040)/Co NPs-NC and BiVO$_4$ (040)/Co SAs-NC, respectively.

The above results demonstrate that BiVO$_4$ (040)/Co SAs-NC photoanode show enhanced charge transfer and charge injection efficiencies based on facet engineering matched with single-atom-Co cocatalyst. It is well known that the measuring photocurrent is equal to the product of theoretical photocurrent, charge separation efficiency and charge injection efficiency. UV–vis diffuse-reflectance spectra prove that the modification of Co SAs-NC does not affect the light absorption of BiVO$_4$ (Fig. 4a). Moreover, the charge separation efficiency of BiVO$_4$ (040)/Co SAs-NC slightly increased, while the charge injection efficiency of BiVO$_4$ (040)/Co SAs-NC has been significant improved compared to pristine BiVO$_4$ (040), as shown in Fig. 4c and Fig. 4d respectively. From the above results, we can conclude that the modification of Co SAs-NC clear increases the activity of BiVO$_4$ by largely enhancing its charge injection efficiency. The mechanism of BiVO$_4$ (040)/Co SAs-NC photoanode is illustrated in Scheme 2. Under illumination, photoexcited holes (h$^+$) and electrons (e$^-$) rapidly migrated to the semiconductor/cocatalyst interface and FTO respectively owing to the faster charge transfer rate of (040) crystallographic orientation BiVO$_4$, and the efficient conductivity N-doped carbon nanosheets. Furthermore, highly exposed (040) facets and cobalt single atoms have high chemical reactivity, which leads to the improvement of hole injection efficiency. The rapid hole injection avoids the excessive accumulation and recombination of holes and ensures the effective utilization of photogenerated charges.
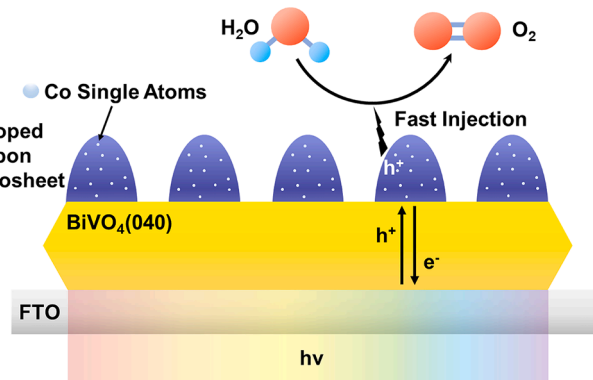
Scheme 2. The schematic diagram of the BiVO$_4$ (040)/Co SAs-NC photoanode under illumination.

5. Conclusions

In conclusion, single-atomic-Co cocatalyst on (040) facet of BiVO$_4$ photoanode has been successfully prepared, in which the highly exposed (040) facets BiVO$_4$ was synthesised by regulating hydrothermal duration and Co SAs-NC cocatalyst loading amount can be facilely controlled by the electrosynthesis time. The XPS and XAS confirm the single-atomic-Co stabilized in BiVO$_4$ (040)/Co SAs-NC by isolated Co–N bonds. The as-prepared BiVO$_4$ (040)/Co SAs-NC presents excellent photocurrent density and nearly 100% charge injection efficiency. The time-resolved transient photoluminescence, EIS and Mott–Schottky measurements reveal that Co SAs-NC facilitate the charge transfer and charge injection of BiVO$_4$ (040). It is expected that the facet engineering strategy and single-atom cocatalyst modification can be applicable to other

photoelectrodes for advanced performance in the field of PEC water splitting.

CRediT authorship contribution statement

Yucong Miao: Investigation, Methodology, Validation, Visualization. **Jingchao Liu:** Methodology, Visualization. **Lixun Chen:** Methodology, Validation. **He Sun:** Methodology, Validation. **Ruikang Zhang:** Investigation, Funding acquisition, Writing - original draft. **Jian Guo:** Investigation, Supervision, Writing - review & editing. **Mingfei Shao:** Supervision, Funding acquisition, Writing - review & editing, Project administration.

Declaration of Competing Interest

The authors declare that they have no known competing financial interests or personal relationships that could have appeared to influence the work reported in this paper.

Acknowledgements

Appendix A. Supplementary data

Supplementary data to this article can be found online at https://doi.org/10.1016/j.cej.2021.131011.

References

[1] C. Ding, J. Shi, Z. Wang, C. Li, Photoelectrocatalytic water splitting: significance of cocatalysts, electrolyte, and interfaces, ACS Catal. 7 (2017) 675–688.

[2] X. Sheng, T. Xu, X. Feng, Rational design of photoelectrodes with rapid charge transport for photoelectrochemical applications, Adv. Mater. 31 (2019) 1805132.

[3] S. Chen, D. Huang, P. Xu, W. Xue, L. Lei, M. Cheng, R. Wang, X. Liu, R. Deng, Semiconductor-based photocatalysts for photocatalytic and photoelectrochemical water splitting: will we stop with photocorrosion, J. Mater. Chem. A 8 (5) (2020) 2286–2322.

[4] M. Li, H.-J. Wang, C. Zhang, Y.-B. Chang, S.-J. Li, W. Zhang, T.-B. Lu, Enhancing the photoelectrocatalytic performance of metal-free graphdiyne-based catalyst, Sci. China Chem. 63 (8) (2020) 1040–1045.

[5] D.K. Lee, D. Lee, M.A. Lumley, K.-S. Choi, Progress on ternary oxide-based photoanodes for use in photoelectrochemical cells for solar water splitting, Chem. Soc. Rev. 48 (7) (2019) 2126–2157.

[6] X. Huang, Y. Li, X. Gao, Q. Xue, R. Zhang, Y. Gao, Z. Han, M. Shao, The effect of the photochemical environment on photoanodes for photoelectrochemical water splitting, Dalton Trans. 49 (35) (2020) 12338–12344.

[7] W. Li, L. Du, Q. Liu, Y. Liu, D. Li, J. Li, Trimetallic oxyhydroxide modified 3D coral-like BiVO₄ photoanode for efficient solar water splitting, Chem. Eng. J. 384 (2020), 123323.

[8] Y. Li, R. Zhang, J. Li, J. Liu, Y. Miao, J. Guo, M. Shao, TiO₂/CuPc/NiFe-LDH photoanode for efficient photoelectrochemical water splitting, Chin. Chem. Lett. 32 (3) (2021) 1165–1168.

[9] Z. Kang, H. Si, S. Zhang, J. Wu, Y. Sun, Q. Liao, Z. Zhang, Y. Zhang, Interface engineering for modulation of charge carrier behavior in ZnO photoelectrochemical water splitting, Adv. Funct. Mater. 29 (2019) 1808032.

[10] Y. Chen, L. Wang, R. Gao, Y.-C. Zhang, L. Pan, C. Huang, K. Liu, X.-Y. Chang, X. Zhang, J.-J. Zou, Polarization-Enhanced direct Z-scheme ZnO-WO₃₋ₓ nanorod arrays for efficient piezoelectric-photoelectrochemical Water splitting, Appl. Catal. B Environ. 259 (2019), 118079.

[11] S.S. Kalanur, H. Seo, Intercalation of barium into monoclinic tungsten oxide nanoplates for enhanced photoelectrochemical water splitting, Chem. Eng. J. 355 (2019) 784–796.

[12] H. Zhang, W.Y. Noh, F. Li, J.H. Kim, H.Y. Jeong, J.S. Lee, Three birds, one-stone strategy for hybrid microwave synthesis of Ta and Sn codoped Fe₂O₃@FeTaO₄ nanorods for photo-electrochemical water oxidation, Adv. Funct. Mater. 29 (2019) 1805737.

[13] N.D. Quang, W. Hu, H.S. Chang, P.C. Van, D.D. Viet, J.-R. Jeong, D.-B. Seo, E.-T. Kim, C. Kim, D. Kim, Fe₂O₃ hierarchical tubular structure decorated with cobalt phosphide (CoP) nanoparticles for efficient photoelectrochemical water splitting, Chem. Eng. J. 417 (2021), 129278.

[14] S. Wang, P. Chen, J.-H. Yun, Y. Hu, L. Wang, An electrochemically treated BiVO₄ photoanode for efficient photoelectrochemical water splitting, Angew. Chem. Int. Ed. 56 (29) (2017) 8500–8504.

[15] C.S. Yaw, J. Tang, A.K. Soh, M.N. Chong, Synergistic effects of dual-electrocatalyst FeOOH/NiOOH thin films as effective surface photogenerated hole extractors on a novel hierarchical heterojunction photoanode structure for solar-driven photoelectrochemical water splitting, Chem. Eng. J. 380 (2020), 122501.

[16] J. Jian, Y. Xu, X. Yang, W. Liu, M. Fu, H. Yu, F. Xu, F. Feng, L. Jia, D. Friedrich, R. van de Krol, H. Wang, Embedding laser generated nanocrystals in BiVO₄ photoanode for efficient photoelectrochemical water splitting, Nat. Commun. 10 (2019) 2609.

[17] Z.-F. Huang, L. Pan, J.-J. Zou, X. Zhang, L. Wang, Nanostructured bismuth vanadate-based materials for solar-energy-driven water oxidation: a review on recent progress, Nanoscale 6 (2014) 14044–14063.

[18] K.K. Dey, S. Gahlawat, P.P. Ingole, BiVO₄ optimized to nano-worm morphology for enhanced activity towards photoelectrochemical water splitting, J. Mater. Chem. A 7 (37) (2019) 21207–21221.

[19] J. Liu, J. Li, Y. Li, J. Guo, S.-M. Xu, R. Zhang, M. Shao, Photoelectrochemical water splitting coupled with degradation of organic pollutants enhanced by surface and interface engineering of BiVO₄ photoanode, Appl. Catal. B Environ. 278 (2020), 119268.

[20] D. Xu, T. Xia, H. Xu, W. Fan, W. Shi, Synthesis of ternary spinel MCo₂O₄ (M = Mn, Zn)/BiVO₄ photoelectrodes for photolectrochemical water splitting, Chem. Eng. J. 392 (2020), 124838.

[21] S. Jin, X. Ma, J. Pan, C. Zhu, S.E. Saji, J. Hu, X. Xu, L. Sun, Z. Yin, Oxygen vacancies activating surface reactivity to favor charge separation and transfer in nanoporous BiVO₄ photoanodes, Appl. Catal. B Environ. 281 (2021), 119477.

[22] J. Jian, G. Jiang, R. van de Krol, B. Wei, H. Wang, Recent advances in rational engineering of multinary semiconductors for photoelectrochemical hydrogen generation, Nano Energy 51 (2018) 457–480.

[23] S. Wang, G. Liu, L. Wang, Crystal facet engineering of photoelectrodes for photoelectrochemical water splitting, Chem. Rev. 119 (8) (2019) 5192–5247.

[24] S. Chen, D. Huang, P. Xu, X. Gong, W. Xue, L. Lei, R. Deng, J. Li, Z. Li, Facet-engineered surface and interface design of monoclinic scheelite bismuth vanadate for enhanced photocatalytic performance, ACS Catal. 10 (2) (2020) 1024–1059.

[25] J. Liu, S.-M. Xu, Y. Li, R. Zhang, M. Shao, Facet engineering of WO₃ arrays toward highly efficient and stable photoelectrochemical hydrogen generation from natural seawater, Appl. Catal. B Environ. 264 (2020), 118540.

[26] L. Mu, Y. Zhao, A. Li, S. Wang, Z. Wang, J. Yang, Y. Wang, T. Liu, R. Chen, J. Zhu, F. Fan, R. Li, C. Li, Enhancing charge separation on high symmetry SrTiO₃ exposed with anisotropic facets for photocatalytic water splitting, Energy Environ. Sci. 9 (7) (2016) 2463–2469.

[27] J. Song, M.J. Seo, T.H. Lee, Y.-R. Jo, J. Lee, T.L. Kim, S.-Y. Kim, S.-M. Kim, S. Y. Jeong, H. An, S. Kim, B.H. Lee, D. Lee, H.W. Jang, B.-J. Kim, S. Lee, Tailoring crystallographic orientations to substantially enhance charge separation efficiency in anisotropic BiVO₄ photoanodes, ACS Catal. 8 (7) (2018) 5952–5962.

[28] M. Shi, G. Li, J. Li, X. Jin, X. Tao, B. Zeng, E.A. Pidko, R. Li, C. Li, Intrinsic facet-dependent reactivity of well-defined BiOBr nanosheets on photocatalytic water splitting, Angew. Chem. Int. Ed. 59 (16) (2020) 6590–6595.

[29] C.W. Kim, Y.S. Son, M.J. Kang, D.Y. Kim, Y.S. Kang, (040)-crystal facet engineering of BiVO₄ plate photoanodes for solar fuel production, Adv. Energy Mater. 6 (2016) 1501754.

[30] K. Zhang, J. Liu, L. Wang, B. Jin, X. Yang, S. Zhang, J.H. Park, Near-complete suppression of oxygen evolution for photoelectrochemical H₂O oxidative H₂O₂ synthesis, J. Am. Chem. Soc. 142 (19) (2020) 8641–8648.

[31] F. Chen, C. Wu, J. Wang, C.P. François-Xavier, T. Wintgens, Highly efficient Z-scheme structured visible-light photocatalyst constructed by selective doping of Ag@AgBr and Co3O4 separately on 010 and 110 facets of BiVO4: pre-separation channel and hole-sink effects, Appl. Catal. B Environ. 250 (2019) 31–41.

[32] K. Zhang, B. Jin, C. Park, Y. Cho, X. Song, S. Zhang, W. Kim, H. Zeng, J. H. Park, Black phosphorene as a hole extraction layer boosting solar water splitting of oxygen evolution catalysts, Nat. Commun. 10 (2019) 2001.

[33] Z. Xu, Z. Fan, Z. Shi, M. Li, J. Feng, L. Pei, C. Zhou, J. Zhou, L. Yang, W. Li, G. Xu, S. Yan, Z. Zou, Interface manipulation to improve plasmon-coupled photoelectrochemical water splitting on alpha-Fe₂O₃ photoanodes, ChemSusChem. 11 (2018) 237–244.

[34] X. Deng, D.C. Sorescu, I. Waluyo, A. Hunt, D.R. Kauffman, Bulk vs intrinsic activity of NiFeOₓ electrocatalysts in the oxygen evolution reaction: the influence of catalyst loading, morphology, and support material, ACS Catal. (2020) 11768–11778.

[35] X. Yang, L. Li, Z. Yang, J. Hu, Y. Lei, P. Li, Z. Zheng, Charge reactions on crystalline/amorphous lanthanum nickel oxide cocatalyst modified hematite photoanode, J. Chem. Phys. 153 (2020), 024701.

[36] J. Xu, Y. Song, H. Wu, J. Liu, Probing the catalytic behavior of ZnO nanowire supported Pd₁ single-atom catalyst for selected reactions, Chin. J. Catal. 38 (9) (2017) 1549–1557.

[37] W. Liu, L. Cao, W. Cheng, Y. Cao, X. Liu, W. Zhang, X. Mou, L. Jin, X. Zheng, W. Che, Q. Liu, T. Yao, S. Wei, Single-site active cobalt-based photocatalyst with a long carrier lifetime for spontaneous overall water splitting, Angew. Chem. Int. Ed. 56 (32) (2017) 9312–9317.

[38] J. Wang, Z. Li, Y. Wu, Y. Li, Fabrication of single-atom catalysts with precise structure and high metal loading, Adv. Mater. 30 (2018) 1801649.

[39] J. Li, C. Zhang, H. Ma, T. Wang, Z. Guo, Y. Yang, Y. Wang, H. Ma, Modulating interfacial charge distribution of single atoms confined in molybdenum phosphosulfide heterostructures for high efficiency hydrogen evolution, Chem. Eng. J. 414 (2021), 128834.

[40] Y. Pang, W. Zang, Z. Kou, L. Zhang, G. Xu, J. Lv, X. Gao, Z. Pan, J. Wang, Y. Wu, Assembling of Bi atoms on TiO$_2$ nanorods boosts photoelectrochemical water splitting of semiconductors, Nanoscale 12 (2020) 4302.

[41] S. Bai, J. Liu, M. Cui, R. Luo, J. He, A. Chen, Two-step electrodeposition to fabricate the p–n heterojunction of a Cu$_2$O/BiVO$_4$ photoanode for the enhancement of photoelectrochemical water splitting, Dalton Trans. 47 (19) (2018) 6763–6771.

[42] D. Li, Y. Liu, W. Shi, C. Shao, S. Wang, C. Ding, T. Liu, F. Fan, J. Shi, C. Li, Crystallographic-orientation-dependent charge separation of BiVO$_4$ for solar water oxidation, ACS Energy Lett. 4 (2019) 825–831.

[43] Q. Song, J. Li, L. Wang, Y. Qin, L. Pang, H. Liu, Stable single-atom cobalt as a strong coupling bridge to promote electron transfer and separation in photoelectrocatalysis, J. Catal. 370 (2019) 176–185.

[44] Z. Li, J. Cui, Y. Liu, J. Li, K. Liu, M. Shao, Electrosynthesis of well-defined metal−organic framework films and the carbon nanotube network derived from them toward electrocatalytic applications, ACS Appl. Mater. Interfaces. 10 (40) (2018) 34494–34501.

[45] W. Xie, Y. Song, S. Li, J. Li, Y. Yang, W. Liu, M. Shao, M. Wei, Single-atomic-Co electrocatalysts with self-supported architecture toward oxygen-involved reaction, Adv. Funct. Mater. 29 (2019) 1906477.

[46] D.H. Lee, M. Kang, S.-M. Paek, H. Jung, Electrochemical hydrogen storage performance of hierarchical Co metal flower-like microspheres, Electrochim. Acta 217 (2016) 132–138.

[47] J. Li, L. Guo, N. Lei, Q. Song, Z. Liang, Metallic Bi nanocrystal-modified defective BiVO$_4$ photoanodes with exposed (040) facets for photoelectrochemical water splitting, ChemElectroChem 4 (11) (2017) 2852–2861.

[48] H. Wang, Y. Wang, Y. Li, X. Lan, B. Ali, T. Wang, Highly efficient hydrogenation of nitroarenes by N-doped carbon-supported cobalt single-atom catalyst in ethanol/water mixed solvent, ACS Appl. Mater. Interfaces 12 (2020) 34021–34031.

[49] G. Wan, P. Yu, H. Chen, J. Wen, C. Sun, H. Zhou, N. Zhang, Q. Li, W. Zhao, B. Xie, T. Li, J. Shi, Engineering single-atom cobalt catalysts toward improved electrocatalysis, Small 14 (2018) 1704319.

[50] L. Yang, L. Shi, D. Wang, Y. Lv, D. Cao, Single-atom cobalt electrocatalysts for foldable solid-state Zn-air battery, Nano Energy 50 (2018) 691–698.

[51] X. Li, T. Zhang, Y. Chen, Y. Fu, J. Su, L. Guo, Hybrid nanostructured Copper(II) phthalocyanine/TiO$_2$ films with efficient photoelectrochemical performance, Chem. Eng. J. 382 (2020), 122783.

[52] X. Zhong, H. He, M. Yang, G. Ke, Z. Zhao, F. Dong, B. Wang, Y. Chen, X. Shi, Y. Zhou, In^{3+}-doped BiVO$_4$ photoanodes with passivated surface states for photoelectrochemical water oxidation, J. Mater. Chem. A 6 (22) (2018) 10456–10465.